Discover Applied Sciences

Research

Hydraulic transient analysis with the Smoothed Particle Hydrodynamics method coupled with unsteady friction model

Almério José Venâncio Pains Soares Pamplona[1] · José Fernandes Júnior[2] · Joel Roberto Guimarães Vasco[2] · Andreia Aoyagui Nascimento[1]

Received: 22 February 2025 / Accepted: 8 May 2025
Published online: 11 June 2025

Abstract
This study employs the Smoothed Particle Hydrodynamics (SPH) method to investigate hydraulic transient phenomena in pipelines. The Corrected SPH (CSPH) technique effectively addresses domain support boundary imbalances, while the introduction of artificial viscosity suppresses spurious oscillations. A thorough assessment of unsteady friction models underscores their accuracy, showing the model based on two empirical coefficients — K_x, influencing the pressure wave damping ratio, and K_t, which governs pressure wave celerity — as the best among the unsteady friction models. The research optimizes critical parameters to minimize discrepancies between numerical simulations and experimental outcomes, revealing the significant effects of coefficients K_x and K_t on the accuracy of simulation responses. Furthermore, the study highlights the importance of Δx, the initial particle spacing, alongside the number of particles, to enhance both accuracy and stability in simulations. The proposed methodology demonstrates promising capabilities in simulating hydraulic transients, offering valuable insights for more precise modeling of fluid dynamics phenomena.

Article Highlights

- New SPH model improves pressure wave predictions in pipelines by combining particle methods with optimized friction parameters.
- Systematic analysis reveals optimal range for model parameters, reducing numerical error in transient simulations.
- Parameter optimization framework provides practical guidelines for accurate hydraulic transient modeling in pipeline systems.

Keywords Water hammer · Unsteady friction model · Smoothed Particle Hydrodynamics

✉ Almério José Venâncio Pains Soares Pamplona, almeriopamplona@gmail.com; ✉ Joel Roberto Guimarães Vasco, joelvasco@ufg.br; ✉ Andreia Aoyagui Nascimento, aanascimento@ufg.br; José Fernandes Júnior, jfslmb@gmail.com | [1]Department of Mechanical Engineering, Federal University of Goiás, Av. Esperança, s/n, Goiânia, GO 74690-900, Brazil. [2]Department of Hydraulics, Federal University of Goiás, Av. Universitária, 1488, Goiânia, GO 74605-220, Brazil.

1 Introduction

Hydraulic transients have been a pivotal area of study since their initial examination by Manebrea [1] and Michaud [2], and they continue to pose significant challenges in contemporary pipeline systems. These sudden changes in flow can cause pressure to fluctuate dramatically, which might put the system's integrity at risk [3]. Frizell [4] and Joukowski [5] independently established a fundamental relationship between pressure changes and velocity variations. Subsequently, Allevi [6, 7] advanced this knowledge by formalizing the general theory through a set of balance equations, showing that the maximum pressure in a system is constrained not to exceed double the static head. The most common one-dimensional set of hyperbolical partial equations modeling the hydraulic transient were set by Streeter and Wylie [8] and Chaudhry [9].

The complexities of modern pipeline systems and increasing operational demands have emphasized the limitations of traditional methods used for hydraulic transient analysis. One approach that has become more popular is the Method of Characteristics (MOC), known for its efficiency and ability to manage various boundary conditions [10]. Gray [11] originally applied the MOC to frictionless pipes, with Lister [12] advancing the approach by popularizing a fixed-grid methodology. Subsequent contributions include Lai [13], who introduced frictional losses into the MOC framework, and Streeter [14], who established boundary conditions for valve operations. An aspect of MOC is its dependence on the stability condition expressed as $c\Delta t/\Delta x = 1$, where c denotes wave speed, Δt represents the time step, and Δx is the mesh characteristic size. This relationship presents difficulties in keeping stability in complex water distribution systems, as different parts may require different time intervals.

Lister [12] proposed line interpolations to approximate head and flow at the base of the characteristic lines to mitigate these challenges. Building on this, Karney and Ghidaoui [15] introduced a hybrid interpolation technique integrating multiple approaches, which optimized memory utilization, execution speed, and the flexibility of discretization in pipe networks. Innovations by Bergant et al. [16, 17] extended the MOC by incorporating fluid–structure interaction (FSI) and addressing transient phenomena such as unsteady friction, cavitation, and viscoelasticity while representing leakage and blockages. Afshar and Rohani [18] proposed an implicit MOC model to overcome the limitations observed in commonly employed MOC frameworks. Jang et al. [19] introduced a quasi-2D methodology based on the MOC, which minimized the number of computational nodes by deriving one-dimensional characteristic equations for pressure and discharge.

The MOC continues encountering challenges in maintaining mass and momentum conservation when dealing with non-uniform Courant numbers. Although interpolation is essential, it introduces non-physical aspects that can lead to artificial damping of the numerical solution. Including the advective acceleration term presents difficulties, resulting in significant errors [20]. Additionally, mesh-based methodologies exhibit limitations in accurately capturing interface phenomena and discrete processes, including column separation, rapid filling, and slug impact [3, 21].

The understanding of unsteady friction has evolved significantly since Schönfeld's [22] pioneering work. Daily et al. [23] introduced their classical empirical model, while Zielke [24] developed an analytical model for laminar flows. Subsequential refinements by Brunone et al. [25], Vardy and Brown [26], and Ramos et al. [27] have improved our ability to model these effects. However, accurately representing unsteady friction remains challenging, particularly in complex flow conditions.

As an alternative, Physics-Informed Neural Networks (PINNs) have shown promise in combining measurement data with conversation laws [28], while machine learning techniques have advanced leak detection capabilities [29]. However, these data-driven approaches frequently depend on extensive training datasets and may not adequately represent the fundamental physical principles.

Other methods for simulating hydraulic transients, such as the Lattice Boltzmann Method (LBM) and Smoothed Particle Hydrodynamics (SPH), are meshless. LBM is a method based on kinetic energy, first used by Cheng et al. (1998) for unsteady flows and improved by Wu et al. [30] for practical usage. Later, Budinski [31] applied LBM to a one-dimensional hydraulic transient, using an adaptative grid independent of the Courant number. Budinski [31] also developed boundary conditions for straight pipes, branching pipes, valve-end pipes, reservoirs, surge tanks, and air chambers. LBM showed favorable performance for low-frequency water hammer but lost stability and performance for high-frequency water hammer cases [32].

Initially developed for astrophysical simulations [33, 34], SPH offers several advantages over traditional grid-based methods: natural handling of complex geometries and moving boundaries, better representation of discontinuities, improved capture of interface phenomena, and flexibility in spatial resolution [35]. Over the years, SPH has been applied in various complex flow scenarios, including solitary wave propagation by Monaghan and Kos [36], sloshing phenomena by Colagrossi et al. [37], hydraulic jumps Federico et al. [38], and dam break events by Monaghan [39]. In the context of hydraulic transients, it was initially introduced by Hou et al. [40] and further validated by Junior et al. [41].

Recent developments have extended SPH capabilities in hydraulic transient analysis. Song et al. [3] applied an SPH-based model combined with MOC for water hammer in water distribution systems, known as SPH-WHWDS. The MOC is used to treat inflow and outflow unknowns at various boundaries, while SPH takes care of the flow within the pipes. Song et al. [21] also advanced mixed-flow modeling using SPH coupled with a two-component pressure approach (SPH-TPA), improving transitions between free-surface and pressurized flows. However, significant challenges remain in accurately representing unsteady friction effects and ensuring numerical stability while maintaining computational efficiency.

Some research on integrating SPH with unsteady friction models has produced successful results. For instance, Pan et al. [42] investigated unsteady friction models using virtual and mirror particles. Their results pointed out the importance of parameter selection, especially artificial viscosity and smoothing length. However, there is still no systematic optimization of these parameters in the existing literature.

The present study addresses unsteady friction accuracy and the lack of systematic optimization parameters by developing a comprehensive SPH model for hydraulic transient analysis coupled with unsteady friction. The approach introduces: integration of Corrected SPH (CSPH) technique to address domain support imbalances, building on theoretical framework established by Chen et al. [43], systematic assessment of unsteady friction models, including those by Vardy and Hwang [44], Vitkovsky et al. [45], and Ramos et al. [27], novel parameter optimization framework using response surface methodology [46], and comprehensive validation against experimental data [47].

This paper is organized as follows: section 2 represents the governing equations and mathematical models for unsteady friction. Section 3 details the implementation of the SPH method, including the smoothing function, domain discretization, and artificial viscosity treatment. Section 4 delineates the experimental setup along with the simulation parameters employed in the study. Section 5 provides an overview of the error metrics applied for validation purposes. Section 6 discusses the results, incorporating an analysis of parameter sensitivity and model performance. Finally, Sect. 7 offers conclusions drawn from the findings and presents recommendations for future investigations.

2 Governing equations

Hydraulic transients in conduits are described by nonlinear partial differential equations based on mass conservation, Eq. (1), and momentum principles, Eq. (2). This mathematical model assumes an incompressible, homogeneous, and isotropic flow.

$$\frac{DH}{Dt} + \frac{c^2}{g}\frac{\partial U}{\partial x} = 0, \tag{1}$$

$$\frac{DU}{Dt} + g\frac{\partial H}{\partial x} + \frac{4\tau}{\rho\, d} = 0, \tag{2}$$

where H signifies the pressure head prevailing within the conduit (m), U designates the mean flow velocity (m/s), c represents the velocity of elastic wave propagation within the fluid medium (m/s), g embodies the gravitational acceleration (m/s^2), ρ is the density (kg/m^3), d is the pipe internal wall diameter (m), and τ is the friction term (Pa). Additionally, x and t correspond to spatial displacement along the conduit axis and the temporal dimension, respectively. The notations $D(\cdot)/Dt$ and $\partial(\cdot)/\partial x$ denote total and partial derivatives, respectively.

2.1 Mathematical models of variable friction

Friction stress τ, Eq. (2), can be decomposed into two components: quasi-stationary friction stress (τ_S) and unsteady friction stress (τ_U). During transient flow, changes in velocity profiles can amplify the dissipation of mechanical energy due to friction and inertial forces, Covas et al. [48]. The quasi-stationary friction stress is described as:

$$\tau_S = \frac{1}{8}\rho\,\lambda\,|U|\,U, \tag{3}$$

where λ represents the quasi-stationary friction factor, which is evaluated using the approximation of [49]:

$$\lambda = \left\{ \left(\frac{64}{Re}\right)^8 + 9.5\left[\ln\left(\frac{\epsilon}{3.7d} + \frac{5.74}{Re^{0.9}}\right) - \left(\frac{2500}{Re}\right)^6\right]^{-16} \right\}^{1/8}, \tag{4}$$

where Re is the Reynolds number, and ϵ is the internal pipe walls' absolute roughness (m).

The unsteady friction stress, based on the study of Zielke [24] for unsteady laminar flow friction, stems from the moment equations of incompressible axially symmetric flow using Laplace transforms, yielding:

$$\tau_U = \frac{4\,\rho\,\nu}{d}\int_0^t \frac{\partial U}{\partial t}(t^*)\phi(t-t^*)\,\mathrm{d}t^*, \tag{5}$$

where ν is the kinematic viscosity, t^* is the instant immediately preceding t, and $\phi(t-t^*)$ is a weighting function that accounts for prior velocity variations, defined as:

$$\phi(t-t^*) = C\sum_{k=1}^{\infty} \exp\left[\eta_k(t-t^*)\right], \tag{6}$$

with C and η_k being constants contingent upon the modeled problem.

Due to computational expenses tied to integrating Eq. (5), Vardy and Hwang [44] propose an approximation:

$$\tau_U = \frac{4\,\nu\,\rho}{d}\left[Y_1(t) + Y_2(t)\right], \tag{7}$$

where the authors derived the temporal expressions, Y_m, for a flow within a laminar ring encompassing a central core of uniform velocity, such that:

$$\phi(\psi) = \frac{\lambda\,Re}{4}\sum_{k=1}^{\infty} \exp\left[-\frac{\psi}{16}(k\,\pi\,\lambda\,Re)^2\right], \tag{8}$$

where ψ is the dimensionless time defined as:

$$\psi = \frac{4\,\nu}{d^2}(t-t^*). \tag{9}$$

The approach introduced by Vardy and Hwang [44] seeks to emulate the exponential behavior of Eq. (8) when integrated with Eq. (5) through the intermediary functions Y_m, Eq. (2.1.8):

$$Y_m(t) = \begin{cases} 0, & t = 0, \\ Y_{m,t-1}\exp\left(-B_m\,\psi\right) + T_m\left(U^t - U^{t^*}\right), & t > 0, \end{cases} \tag{10}$$

where, B_m and T_m are constants computed by minimizing the squared error between $\phi(\psi)$ and Y_m. Additionally, U^t represents the current velocity, and U^{t^*} denotes the velocity at the previous instant. Vardy and Hwang [44] provide pre-calculated values for the constants B_m and T_m for specific ranges of values defined by $\lambda_R\,Re = 0.25\,\lambda\,Re$, as shown in Table 1.

Table 1 Values of the coefficients B_m and T_m for several ranges defined by $\lambda_R Re$

$\lambda_R Re$	T_1	T_2	B_1	B_2
250.000	250.000	74.000	4.400×10^5	4.200×10^5
500.000	260.000	65.000	5.600×10^5	1.150×10^5
1000.000	350.000	65.000	9.800×10^5	4.120×10^5
2000.000	470.000	65.000	2.800×10^5	1.620×10^5

Carstens and Roller [50] introduced a model for unsteady friction stress in 1959, proposing that velocity profiles remain similar under steady-state and unsteady conditions due to the relationship between unsteady stress and local acceleration, resulting in the expression:

$$\tau_U = \frac{K\,\rho\,d}{4}\frac{\partial U}{\partial t}, \tag{11}$$

where K denotes the damping factor. The approach of Carstens and Roller [50] is widely used due to its numerical simplicity and was later improved upon by Brunone et al. [25], resulting in Eq. (12):

$$\tau_U = \frac{K\,\rho\,d}{4}\left(\frac{\partial U}{\partial t} - c\,\frac{\partial U}{\partial x}\right), \tag{12}$$

where the damping factor K is experimentally determined. This revised approach includes a convective term related to the velocity of elastic wave propagation in the fluid, leading to improved agreement with experimental data.

Vardy and Brown [26] justify Eq. (11) by assuming that local acceleration is constant, thus leaving the integral in Eq. (5). From this, they derive an approximation for K:

$$K = 2\sqrt{\theta}, \tag{13}$$

where θ is the shear decay coefficient, a function of the Reynolds number:

$$\theta = \frac{7.41}{Re^{\kappa}}, \tag{14}$$

with $\kappa = \log_{10}\left(14.3Re^{-0.05}\right)$. Equation (13) also holds for Eq. (12) if one assumes that the local acceleration in Eq. (11) corresponds to the unsteady and advective term in Eq. (12).

Due to the numerical implementation challenges of Eq. (12), Vitkovsky et al. [45] proposed the following modification:

$$\tau_U = \frac{K\,\rho\,d}{4}\left(\frac{\partial U}{\partial t} - c\,\mathrm{sgn}(U)\left|\frac{\partial U}{\partial x}\right|\right), \tag{15}$$

where $\mathrm{sgn}(\cdot)$ represents the sign function.

In 2004, Ramos et al. [27] modified the damping factor in Eq. (15) as follows:

$$\tau_U = \frac{\rho\,d}{4}\left(K_t\frac{\partial U}{\partial t} - K_x\,c\,\mathrm{sgn}(U)\left|\frac{\partial U}{\partial x}\right|\right). \tag{16}$$

Ramos et al. [27] used specific coefficients for acceleration terms to control wave phase, K_t, and amplitude damping, K_x: this improved numerical approximations and reduced discrepancies between experimental and numerical results in advanced time steps.

3 SPH method

Smoothed Particle Hydrodynamics (SPH) is grounded in the continuous physical medium discretization using a collection of irrotational and non-deformable particles. These particles are advected by the flow, allowing flow properties to be assessed at the particle positions and computed through interpolation with neighboring particles. This interpolation employs a smoothing function (kernel) without establishing particle connectivity through a mesh.

To discretize a spatially varying quantity f within the continuous domain Ω, the quantity f is first represented through a convolution integral across the continuous domain:

$$\langle f(x)\rangle = \int_{\Omega} f\left(x'\right)W\left(\left|x-x'\right|,h\right)\,\mathrm{d}x' \tag{17}$$

where W denotes the smoothing kernel function, $\mathrm{d}x'$ is the differential volume element, and h is the smoothing length. The parameter h determines the extent of the smoothing function's support domain. The symbol $\langle\cdot\rangle$ signifies an approximation of $f(x)$.

3.1 The smoothing function

The smoothing function governs the degree to which a particle transfers property values such as momentum, energy, or any other attribute to its neighboring particles. Therefore, the accuracy of representing a function under analysis via Eq. (17) hinges on the chosen smoothing function.

The present paper adopted the cubic spline function, Eq. (18), proposed by Monaghan and Lattanzio [51]. This function features a compact domain defined by the radius $s = |x - x'|/h$, as shown in Fig. 1 As the smoothing length approaches zero, it behaves akin to the impulse or Dirac delta function.

$$W(s,h) = \frac{1}{6\,h}\begin{cases} (2-s)^3 - 4(1-s)^3, & 0 \le s < 1, \\ (2-s)^3, & 1 \le s < 2, \\ 0, & s \ge 2. \end{cases} \tag{18}$$

Formula (18) consists of linear functions in its second derivative, which may lead to reduced numerical stability compared to functions with smoother derivatives. A study by Fulk and Quinn [52] supported using the cubic spline smoothing kernel. They examined the effectiveness of different smoothing kernels in one dimension.

3.2 Discretization of government equations

The discretization of the one-dimensional hydraulic transient equations, expressed within the context of the SPH method, commences with the representation of functions and their derivatives in particle form. Consequently, the value of any function $f(x)$ evaluated at particle i, Eq.(17), is given by

$$\left\langle f\left(x_i\right)\right\rangle = \sum_{j=1}^{n_i} f\left(x_j\right) W_{ij}\,\frac{m_j}{\rho_j}, \tag{19}$$

where $W_{ij} = W\left(|x_i - x_j|, h\right)$, m_j represents the mass of each particle, and n_i signifies the number of particles within the compact domain of particle i. Concerning the discretization of the first derivative, we have

$$\left\langle \frac{\partial f\left(x_i\right)}{\partial x}\right\rangle = \sum_{j=1}^{n_i}\left(f\left(x_j\right) - f\left(x_i\right)\right)\frac{\partial W_{ij}}{\partial x}\,\frac{m_j}{\rho_j}, \tag{20}$$

where $\partial W_{ij}/\partial x$ stands for the partial derivative of the kernel calculated over the distance $|x_i - x_j|$ and the smoothing length h.

Upon substituting Eq. (20) into the variables $\partial H/\partial x$ and $\partial U/\partial x$ of Eq.(1) and (2), respectively, the following approximations are obtained for any particle i:

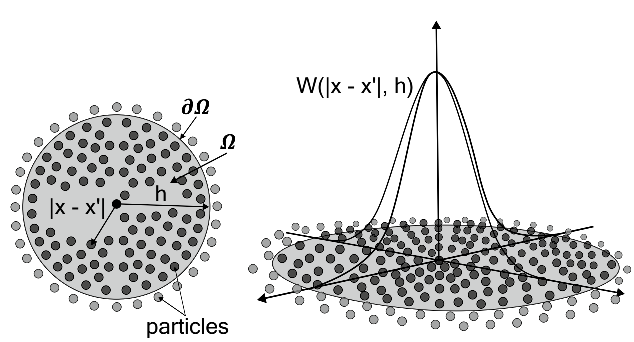

Fig. 1 Scheme of a smoothing function acting on a compact domain with the h radius of an i-th particle

$$\left\langle \frac{DH(x_i,t)}{Dt} \right\rangle = -\frac{c^2}{g} \sum_{j=1}^{n_i} \left(U(x_j,t) - U(x_i,t) \right) \frac{\partial W_{ij}}{\partial x} \frac{m_j}{\rho_j}, \tag{21}$$

$$\left\langle \frac{DU(x_i,t)}{Dt} \right\rangle = -g \sum_{j=1}^{n_i} \left(H(x_j,t) - H(x_i,t) \right) \frac{\partial W_{ij}}{\partial x} \frac{m_j}{\rho_j} - \frac{4 \left\langle \tau(x_i,t) \right\rangle}{\rho\, d}. \tag{22}$$

3.3 Domain discretization

Consistency measures the difference between an approximation and a function's actual value. Zeroth-order consistency is when a technique can accurately approximate a constant function. First-order consistency is when a method can accurately represent a linear function. SPH achieves constant and linear consistency in a continuous domain with convolution integrals. However, particle distribution does not guarantee consistency in a discrete domain [35]. The following conditions must hold for constant consistency in SPH's discrete domain:

$$\sum_{j=1}^{n_i} W_{ij} \frac{m_j}{\rho_j} = 1, \tag{23}$$

whereas linear consistency is attained when

$$\sum_{j=1}^{n_i} \left(x_i - x_j \right) W_{ij} \frac{m_j}{\rho_j} = 0. \tag{24}$$

Equations (23) and (24) show that particles near the boundary of the support domain cause unbalanced contributions, resulting in lower values or non-zero values. Irregular particle distributions exacerbate this issue. Hence, a uniform particle distribution was chosen along the tube, with fixed particles at the reservoir exit and valve and uniformly spaced particles along the pipe, Fig. 2.

Consistency of approximation depends on a balanced particle distribution within the support domain. However, particles near the reservoir and valve have an imbalanced distribution. Hence, the Corrected Smoothed Particle Hydrodynamics (CSPH) corrective method proposed by Chen et al. [43] is applied to mitigate the lack of consistency effects. That involves a Taylor series expansion of a function $f\left(x'\right)$ around a known point x, multiplied by $W\left(|x-x'|,h\right)$ and integrated over x' on both sides. The result is

Fig. 2 Reservoir-pipe-valve scheme with a uniform particle distribution along the pipe

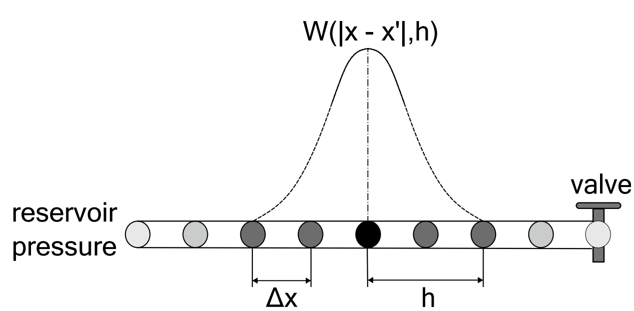

$$\int_{\Omega} f\left(x'\right) W\left(\left|x-x'\right|, h\right) dx' = f(x) \int_{\Omega} W\left(\left|x-x'\right|, h\right) dx' + \frac{\partial f(x)}{\partial x} \int_{\Omega} \left(x-x'\right) W\left(\left|x-x'\right|, h\right) dx' + O\left(h^2\right) \tag{25}$$

The higher-order derivatives in Eq. (25) are disregarded, assuming linear consistency within the support domain due to the symmetry of the smoothing function. Thus, the integral of the first derivative is null, and Eq. (25) is rewritten as

$$\langle f(x) \rangle = \frac{\int_{\Omega} f\left(x'\right) W\left(|x-x'|, h\right) dx'}{\int_{\Omega} W(|x-x'|, h)\, dx'} + O\left(h^2\right). \tag{26}$$

Equation (26) features truncation errors of order h^2 for particles within the support domain due to Taylor expansion truncation. However, particles near the edge exhibit truncation errors of order h, as linear consistency is not respected in this region, leading to a non-zero integral of the first derivative in Eq. (25). Similarly, the first derivative, $\partial f(x)/\partial x$, can also be corrected, assuming the form

$$\left\langle \frac{\partial f(x)}{\partial x} \right\rangle = \frac{\int_{\Omega} \left[f(x') - f(x)\right] \frac{\partial W\left(\left|x-x'\right|, h\right)}{\partial x'} dx'}{\int_{\Omega} (x-x') \frac{\partial W(|x-x'|, h)}{\partial x'} dx'} + O\left(h^2\right). \tag{27}$$

By applying particle discretization within the support domain of the function $f(x)$, Eq. (26) and (27) can be rewritten for the i-th particle as

$$\left\langle f\left(x_i\right) \right\rangle = \frac{\sum_{j=1}^{n_i} \left(fx_j\right) W_{ij} \frac{m_j}{\rho_j}}{\sum_{j=1}^{n_i} W_{ij} \frac{m_j}{\rho_j}}, \tag{28}$$

$$\left\langle \frac{\partial f\left(x_i\right)}{\partial x} \right\rangle = \frac{\sum_{j=1}^{n_i} \left(f\left(x_j\right) - f\left(x_i\right)\right) \frac{\partial W_{ij}}{\partial x} \frac{m_j}{\rho_j}}{\sum_{j=1}^{n_i} \left(x_i - x_j\right) \frac{\partial W_{ij}}{\partial x} \frac{m_j}{\rho_j}}. \tag{29}$$

Given the numerically corrected approximations via the CSPH method, Eq (21) and (22) are rearranged as follows:

$$\left\langle \frac{DH_i^t}{Dt} \right\rangle = -\frac{c^2}{g} \frac{\sum_{j=1}^{n_i} \left(U_j^t - U_i^t\right) \frac{\partial W_{ij}^t}{\partial x} \frac{m_j}{\rho_j}}{\sum_{j=1}^{n_i} \left(x_i^t - x_j^t\right) \frac{\partial W_{ij}^t}{\partial x} \frac{m_j}{\rho_j}}, \tag{30}$$

$$\left\langle \frac{DU_i^t}{Dt} \right\rangle = -g \frac{\sum_{j=1}^{n_i} \left(H_j^t - H_i^t\right) \frac{\partial W_{ij}^t}{\partial x} \frac{m_j}{\rho_j}}{\sum_{j=1}^{n_i} \left(x_i^t - x_j^t\right) \frac{\partial W_{ij}^t}{\partial x} \frac{m_j}{\rho_j}} - \frac{4 \left\langle \tau_i^t \right\rangle}{\rho\, d}. \tag{31}$$

By discretizing the SPH model for the local and convective derivatives of the unsteady friction models by Vardy and Hwang [44], Brunone et al. [25], and Ramos et al. [27], the following expressions are obtained:

$$Y_m(t) = \begin{cases} 0, & t = 0, \\ Y_{m,t-1} \exp\left(-B_m \psi\right) + T_m \left\langle \frac{DU_i^{t-1}}{Dt} \right\rangle \Delta t, & t > 0. \end{cases} \tag{32}$$

$$\tau_{U,i}^{t}=\frac{K\,\rho\,d}{4}\left(\left\langle\frac{DU_i^{t-1}}{Dt}\right\rangle+\frac{g}{c}\,\mathrm{sgn}\left(U_i^t\right)\left\langle\frac{DH_i^t}{Dt}\right\rangle\right), \tag{33}$$

$$\tau_{U,i}^{t}=\frac{\rho\,d}{4}\left(K_t\left\langle\frac{DU_i^{t-1}}{Dt}\right\rangle+K_x\frac{g}{c}\,\mathrm{sgn}\left(U_i^t\right)\left\langle\frac{DH_i^t}{Dt}\right\rangle\right). \tag{34}$$

Here, the superscript t denotes the current time, $t-1$ is equivalent to $t-\Delta t$, and Eq. (30) and (31) give the approximations of derivatives.

3.4 Artificial viscosity

In physical phenomena involving shock waves, the SPH method and its variants develop non-physical oscillations in numerical results near regions where shock waves occur. That is due to the discontinuity generated by the shock wave, a consequence of the transformation of kinetic energy into thermal energy. Apart from oscillations, these discontinuities lead to non-physical particle penetration, causing particles to overlap. According to Liu and Liu [35], to mitigate these issues, a dissipative term is added to represent the energy transformation of momentum caused by shock waves. Therefore, Eq. (31) is rewritten as

$$\left\langle\frac{DU_i^t}{Dt}\right\rangle=-g\,\frac{\sum_{j=1}^{n_i}\left(H_j^t-H_i^t\right)\frac{\partial W_{ij}^t}{\partial x}\frac{m_j^t}{\rho_j^t}}{\sum_{j=1}^{n_i}\left(x_i^t-x_j^t\right)\frac{\partial W_{ij}^t}{\partial x}\frac{m_j^t}{\rho_j^t}}-\frac{4\left\langle\tau_i^t\right\rangle}{\rho\,d}-\sum_{j=1}^{n_i}\Pi_{ij}^t\frac{\partial W_{ij}^t}{\partial x}m_j^t, \tag{35}$$

where Π_{ij} is a term functioning as artificial viscosity, proposed by Monaghan and Gingold [53] and improved by Monaghan [54], as follows:

$$\Pi_{ij}^t=\begin{cases}\frac{\beta\,\zeta_{ij}^2-\alpha\,c\,\zeta_{ij}}{\rho}, & U_{ij}^t\,x_{ij}^t<0,\\ 0, & U_{ij}^t\,x_{ij}^t\geq 0.\end{cases} \tag{36}$$

where α is a constant associated with volumetric viscosity, β is a constant regulating the suppression of particle interpenetration, $U_{ij}^t=U_i^t-U_j^t$, $x_{ij}^t=x_i^t-x_j^t$, and ζ_{ij} is an average velocity defined by

$$\zeta_{ij}=\frac{h}{\left(x_{ij}^t\right)^2}\,U_{ij}^t\,x_{ij}^t. \tag{37}$$

3.5 Time integration

A conditionally stable Euler forward scheme with first-order accuracy was used to integrate the particle pressure and velocity in time [40, 3]:

$$H_i^{t+1}=H_i^t+\left\langle\frac{DH_i^t}{Dt}\right\rangle\Delta t, \tag{38}$$

$$U_i^{t+1}=U_i^t+\left\langle\frac{DU_i^t}{Dt}\right\rangle\Delta t, \tag{39}$$

Table 2 Experimental setup

Test	$Q_0\ (10^{-3}\,\mathrm{m}^3/\mathrm{s})$	H_R	Re_0
1	0.1330	44.6400	8141.3900
2	0.0850	45.5900	5203.1400

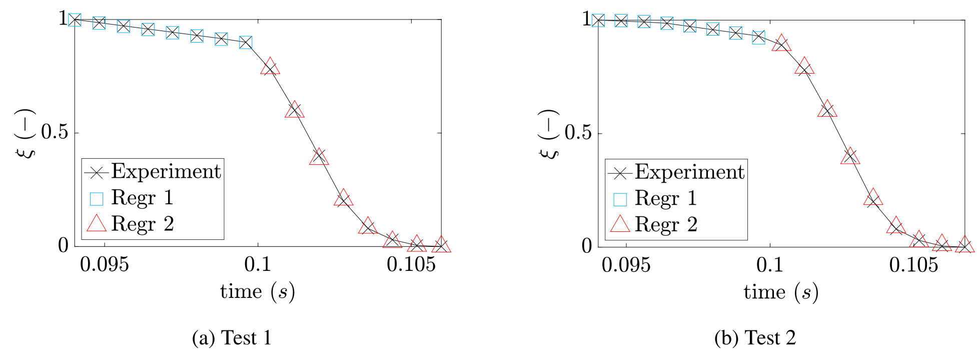

Fig. 3 Valve opening coefficient values throughout valve closure

4 Experimental and simulation setup

The validation of the present work is accomplished through comparisons between numerical results and experimental data presented by Soares et al. [47], using an experimental setup comprising a typical reservoir-pipe-valve configuration as assembled by Martins et al. [55].

The hydro-pneumatic reservoir is maintained at a constant level of H_R and is connected to a copper pipe with a wall thickness $\epsilon = 0.006$ mm, diameter $d = 0.0200$ m, and length $L = 15.2200$ m. A spherical valve is positioned downstream in the pipe, acting as a generator of transients due to the abrupt interruption of steady-state flow (Q_0). Soares et al. [47] placed pressure transducers immediately upstream of the valve and halfway along the pipe, 7.6100 m upstream from the valve. The authors estimated the speed of sound at 1255 m/s based on the experimentally measured time between pressure peaks.

The reservoir upstream of the pipe has much larger dimensions than the pipe, $H_R \gg d$, so the manometric height in the reservoir H_R does not vary during the transient.

The experimental tests conducted by Soares et al. [47] used the initial configurations highlighted in Table 2:

Martins et al. [55] modeled the valve as a free discharge, so the discharged flow (Q) and manometric height (H) are related by the orifice equation:

$$Q = C_D A \sqrt{2 g H}, \tag{40}$$

where C_D is the valve discharge coefficient, A is the effective cross-sectional area of flow in the valve (m^2), and H is the manometric height (m). Knowing that the experiment is initially maintained under steady-state conditions with a flow rate Q_0 and the manometric height in the reservoir H_R, C_D can be determined as a function of Q_0 and H_R through Eq. (40), resulting in:

$$Q = \xi Q_0 \sqrt{\frac{H}{H_R}}, \tag{41}$$

where ξ is a valve opening coefficient, defined by Soares et al. [56] as:

$$\xi = \frac{C_D A}{C_{D,0} A_0}, \tag{42}$$

with $C_{D,0}$ and A_0 being the coefficient and cross-sectional area of the fully open valve state, and C_D and A being the values in other valve states. In particular, $\xi = 1$for the fully open valve and $\xi = 0$ for the fully closed valve. Figure 3 features the ξ experimental behavior data against linear regression curves, Regr1 and Regr2.

The characteristic curve of ξ can be divided into two phases: smooth closure (Regr1) and abrupt closure (Regr2). In the first phase, results were modeled using a first or second-order polynomial. In contrast, in the second phase, a more complex function is necessary, such as a third or fourth-order polynomial. Through linear regression, the following curves for the first experiment were determined:

$$\xi_1 = -17.77916\, t + 2.67200, \tag{43}$$

$$\begin{aligned} \xi_2 = &-2092549041.14908\, t^4 + 865545958.63251\, t^3 \\ &- 134207031.59252\, t^2 + 9245082.87103\, t - 238728.16756, \end{aligned} \tag{44}$$

where Eqs. (43) and (44) have R^2 equal to 0.9999 and 0.9997, respectively, while for the second experiment:

$$\xi_1 = -2682.99544\, t^2 + 505.69584\, t - 22.83048 \tag{45}$$

$$\begin{aligned} \xi_2 = &-2193743122.58627\, t^4 + 914377413.83069\, t^3 \\ &- 142870719.15816\, t^2 + 9917887.49925\, t - 258083.78301. \end{aligned} \tag{46}$$

where Eqs. (45) and (46) have R^2 equal to 0.9999 and 0.9998, respectively. Adequate control of the valve closure allows for simulating the initial conditions of the disturbance inserted into the transient phenomenon with greater fidelity. It is critical that the coefficients of the polynomials remain precise and are not truncated or conveyed in fewer digits, as this can significantly impact the outcomes related to the first peak pressure wave. Additionally, the implementation of overfitting may be required to ensure the accuracy of the valve closure.

Regarding the simulation settings, the current study chose a time step as a multiple of the experimental acquisition resolution. The resolution is 3.3400×10^{-4} s, while $\Delta t = 1.5905 \times 10^{-5}$ s. As for the spatial step, to maintain the Courant-Friedrichs-Lewy (CFL) number equal to unity, it was defined as $\Delta x = 0.0200$ m. Therefore, the total number of particles is, the integer derived from the relationship between Δx and the pipe length, $N = 762$. The mass of each particle is calculated from the relation $m_j = 20$ kg.

Table 3 contains the remaining simulation inputs, except for the smoothing length. This one, we defined as a multiple of Δx, $h = \kappa\, \Delta x$, where $\kappa = 1.2000$ in this work.

The simulation was conducted based on the number of time steps, so we must define the instant at which the valve initiates movement, the instant at which the coefficient of opening behavior changes, and the final instant of closure as the number of time steps. From Fig. 3, one observes these points regarding time. By converting the valve closure's start, transition, and endpoints using 1.5905×10^{-5} s, the values in Table 4 are obtained for each experiment. The simulation comprises 10^5 steps, representing 1.5905 s.

Furthermore, the Euler method was employed for the temporal integration of manometric height and velocity field. The positions of the particles remain constant throughout the simulation.

Table 3 Physical and numerical variables used in the simulation

Physical variables		Numerical variables	
Variable	Value	Variable	Value
ρ_j	$1000\ \mathrm{kg/m^3}$	α	0.6000
g	$9.8060\ \mathrm{m/s^2}$	β	0.0000
ϵ	6.0000×10^{-6} m	K	0.0150
c	1255 m/s	K_t	−0.0180
ν	$1.0400 \times 10^{-6}\ \mathrm{m^2/s}$	K_x	0.0150
m_j	20 kg	Δx	0.0200 m
d	0.0200 m	Δt	1.5905×10^{-5} s
L	15.2200 m	N	762

Table 4 Value of the number of steps that characterize the closing movement of the valve

Test	Begin	Transition	Ending
1	5912	6262	6663
2	5912	6262	6713

5 Error metrics

The numerical accuracy is assessed through the relative error based on the quadratic norm (L_2) and the mean absolute scaled error (*MASE*), described as follows:

$$L_2 = \sqrt{\frac{\sum_{j=1}^{T} \left(f_j - \langle f_j \rangle\right)^2}{\sum_{j=1}^{T} f_j^2}}, \tag{47}$$

$$MASE = \frac{\frac{1}{T}\sum_{j=1}^{T} \left| f_j - \langle f_j \rangle \right|}{\frac{1}{T}\sum_{j=1}^{T} \left| f_j - \bar{f} \right|}, \tag{48}$$

where T is the total number of observed points, $\langle f \rangle$ is the approximated value, f is the real value, and $\bar{f}$ is the mean value of f.

6 Results

6.1 Simulations

Simulation results based on initial data from Table 3 and considering only quasi-stationary friction stress are shown in Figs. 4 and 5. The SPH method captures essential characteristics of the first wave crest from experimental results. However, an accurate representation of the observed wave phase is achieved only until around 0.7 s. Beyond this point, numerical phase lag increases progressively.

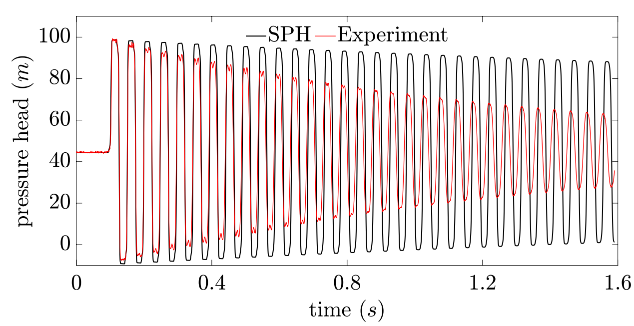

Fig. 4 Numerical result considering only the steady friction model for Test 1

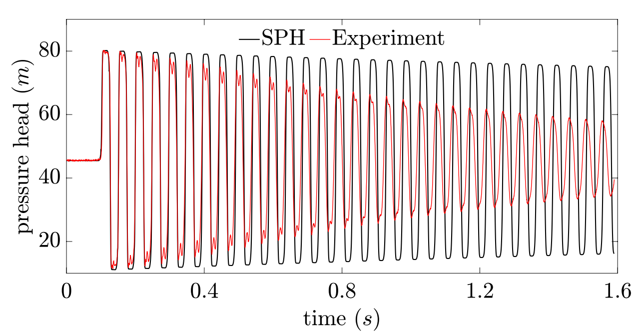

Fig. 5 Numerical result considering only the steady friction model for Test 2

Figure 6 shows the pressure head over the entire simulated interval for Test 1, obtained by incorporating unsteady friction models with numerical variables from Tables 1 and 3. The models exhibit a damping effect similar to the experimental outcome. The model by Ramos et al. [27] maintains a phase of the manometric height signal that closely resembles the testing phase (Fig. 7).

Between 0.2500 s and 0.3000 s, the models proposed by Vardy and Hwang [44] and Brunone et al. [25] exhibit a phase shift, which becomes significantly more pronounced over time. This shift becomes evident as the last observed crest presents an approximately 90° phase difference, as shown in Fig. 8. The waveform smoothing occurs during the phenomenon, and none of the models captured it accurately. The wave transitions from a rectangular nature to a sinusoidal shape at $t = 1.0$ s. The models by Ramos et al. [27] and Vitkovsky et al. [45] maintain a rectangular profile, whereas the model by Vardy and Hwang [44] resembles a smoothed sawtooth waveform.

The numerical results were analyzed using Eq. 47 and 48, and the findings were presented in Table 5. According to the table, the model proposed by Ramos et al. [27] demonstrated the highest accuracy, with L_2 norm errors ranging between 0.120 and 0.180. In contrast, the other models exhibited errors in the range of (0.470, 0.540). The maximum *MASE* observed for the model proposed by Ramos et al. [27] was 33.48%, while the variations in the other models were approximately 90.00%, almost three times higher. The visual assessment of Fig. 6 further supports the superior performance of the model proposed by Ramos et al.[27] in error metrics compared to the other two models. The figure shows

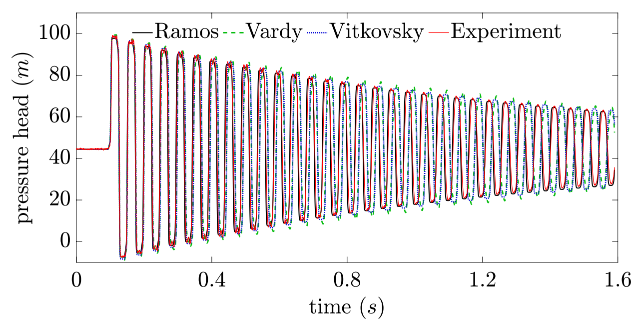

Fig. 6 Numerical result by adding the three unsteady friction models with the test 1 data, overall viewing

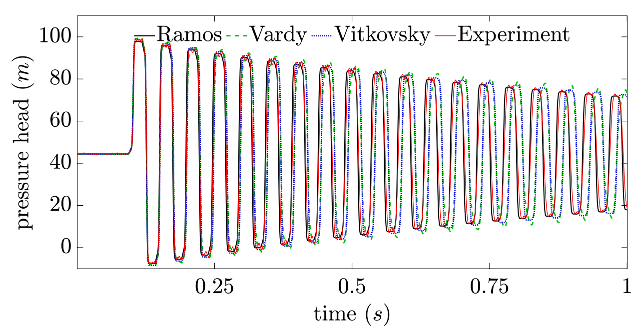

Fig. 7 Numerical result by adding the three unsteady friction models with the test 1 data, a close-up between 0.0 and 1.0 s

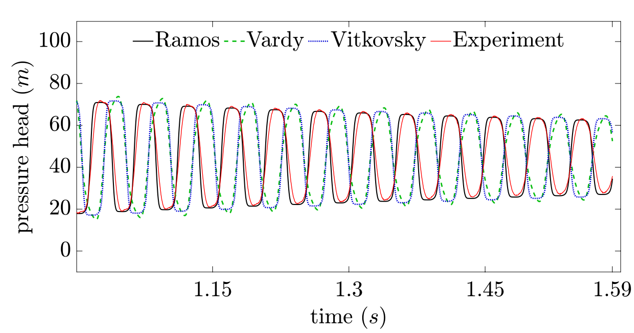

Fig. 8 Numerical result by adding the three unsteady friction models with the test 1 data, a close-up between 1 and 1.6 s

Table 5 Error metrics applied to each the unsteady friction models

Models	L_2	*MASE*
Test 1		
Vardy	0.517	0.869
Vitkovský	0.531	0.878
Ramos	0.128	0.166
Test 2		
Vardy	0.474	0.899
Vitkovský	0.479	0.898
Ramos	0.178	0.335

an improved adherence between the numerical and experimental phases, which is attributed to the independent control of the influence of local acceleration on unsteady friction, as provided by the coefficient K_t.

Despite the accuracy achieved with the model proposed by Ramos et al. [27], the model will eventually exhibit significant phase differences between the numerical and experimental waves. One possible reason for these disparities is the neglect of fluid–structure interaction. Another factor is the simplification of the phenomenon into a one-dimensional problem. In the three-dimensional phenomenon, vortex sheets form near the wall and spread radially toward the center of the tube. These three-dimensional structures emerge during the flow inversion caused by the shock wave front [55].

Additionally, the flow comprises two distinct regions: the wall and the center. In the former, there are intense velocity gradients with rapid changes in velocity profile. In contrast, in the latter, the velocity profile depends mainly on inertial forces and accumulates configurations from previous moments. It would be possible to capture the influences of the two different flow regions with a two-dimensional approach to the numerical model. However, only the three-dimensional numerical model can accurately represent the vortex sheets.

6.2 Analysis of the variables' effects

The study examined the SPH method variables using the statistical technique of response surface methodology with two levels of values for each variable to establish the optimal configuration and understand the impact of each variable on the numerical outcome [46].

Utilizing response surface methodology, various selected variables, including $\Delta x, \alpha, \kappa, K_t$, and K_x, were applied. The coefficient β was disregarded as the model did not involve particle displacement. A constant time maintains consistency among the time step, acquisition resolution, and pressure wave velocity. Since the volumetric flow rate of the tests is a fixed parameter, each test was treated as a replicate, and blocking was applied among them. The response was evaluated as the relative L_2 error.

For a complete experiment with five variables, two replicates, and blocking each, the standard approach includes 32 cubic points, 10 central cubic points, and 10 axial points, resulting in 104 tests. In this study, 52 simulations were conducted by choosing combinations through D-optimization, which minimizes the variance of coefficients obtained through linear regression of estimated parameterized effects of a 2^k experiment. The optimization process maximizes the determinant of the square matrix of effects [46]. Table 6 lists all the selected combinations, levels of each variable, and corresponding responses obtained.

Response surface methodology uses linear regression to construct a surface from Table 6. As a result, the desired equation is a second-order polynomial with interaction terms, using it to calculate the normalized effects of each term and plot them against the Gaussian distribution line to determine their significance. Figure 9 shows that the most significant terms are K_x, $K_x\,K_x$, and K_t. Thus, a surface containing only these terms is assumed, leading to the linear regression equation:

$$\langle L_2 \rangle = 0.5517 - 23.19\,K_x + 33.68\,K_t + 600.6\,K_x^2 + 1145.1\,K_t^2. \tag{49}$$

Equation (49) has positive coefficients in its quadratic terms, indicating a global minimum. The contours of the upward-facing parabolic surface in Fig. 10 reveal that the minimum error occurs at $K_x = 0.0193$ and $K_t = -0.0147$. However, the aim is to provide a minimum value for every variable. Thus, using Eq. (50) with $\alpha = 0.8, K_x = 0.01997, K_t = -0.0149, \Delta x = 0.0116$, and $\kappa = 1.4$, the error prediction is minimized to 0.0528 with 95% confidence in the range of $(-0.0422, 0.1499)$.

Table 6 Experimental design table with the MASE response for the RSM

Block	α	K_x	K_t	Δx	κ	Error L_2
1	0.1000	0.0150	−0.0150	0.0175	1.2250	0.1078
1	0.3000	0.0100	−0.0200	0.0150	1.1500	0.2082
1	0.3000	0.0100	−0.0200	0.0150	1.3000	0.2060
1	0.3000	0.0100	−0.0100	0.0200	1.3000	0.1794
1	0.3000	0.0200	−0.0200	0.0200	1.3000	0.1584
1	0.3000	0.0200	−0.0200	0.0150	1.1500	0.1544
1	0.3000	0.0200	−0.0100	0.0150	1.1500	0.1277
1	0.4500	0.0030	−0.0150	0.0175	1.2250	0.2675
1	0.4500	0.0150	−0.0270	0.0175	1.2250	0.2957
1	0.4500	0.0150	−0.0150	0.0175	1.0500	0.0959
1	0.4500	0.0150	−0.0150	0.0175	1.2250	0.0917
1	0.4500	0.0150	−0.0150	0.0175	1.4000	0.0910
1	0.4500	0.0150	−0.0150	0.0235	1.2250	0.0862
1	0.4500	0.0150	−0.0150	0.0235	1.2250	0.0862
1	0.4500	0.0150	−0.0030	0.0175	1.2250	0.2702
1	0.4500	0.0270	−0.0150	0.0175	1.2250	0.1221
1	0.6000	0.0100	−0.0200	0.0150	1.1500	0.1997
1	0.6000	0.0100	−0.0200	0.0200	1.1500	0.2063
1	0.6000	0.0100	−0.0200	0.0200	1.3000	0.2037
1	0.6000	0.0100	−0.0100	0.0150	1.1500	0.1856
1	0.6000	0.0100	−0.0100	0.0150	1.3000	0.1832
1	0.6000	0.0200	−0.0200	0.0150	1.3000	0.1448
1	0.6000	0.0200	−0.0200	0.0200	1.1500	0.1543
1	0.6000	0.0200	−0.0100	0.0150	1.3000	0.1235
1	0.6000	0.0200	−0.0100	0.0150	1.1500	0.1238
1	0.6000	0.0200	−0.0100	0.0200	1.1500	0.1123
2	0.1000	0.0150	−0.0150	0.0175	1.2250	0.1078
2	0.3000	0.0100	−0.0200	0.0200	1.3000	0.1394
2	0.3000	0.0100	−0.0100	0.0150	1.3000	0.1492
2	0.3000	0.0100	−0.0100	0.0200	1.1500	0.1409
2	0.3000	0.0200	−0.0200	0.0150	1.3000	0.0955
2	0.3000	0.0200	−0.0200	0.0200	1.1500	0.0999
2	0.3000	0.0100	−0.0100	0.0150	1.1500	0.1501
2	0.3000	0.0200	−0.0100	0.0150	1.3000	0.1024
2	0.3000	0.0200	−0.0100	0.0200	1.1500	0.1020
2	0.3000	0.0200	−0.0100	0.0200	1.3000	0.0942
2	0.3000	0.0100	−0.0200	0.0200	1.1500	0.1410
2	0.4500	0.0030	−0.0150	0.0175	1.2250	0.1938
2	0.4500	0.0150	−0.0270	0.0175	1.2250	0.1926
2	0.4500	0.0150	−0.0150	0.0116	1.2250	0.0678
2	0.4500	0.0150	−0.0150	0.0116	1.2250	0.0678
2	0.4500	0.0150	−0.0150	0.0175	1.0500	0.0689
2	0.4500	0.0150	−0.0150	0.0175	1.2250	0.0659
2	0.4500	0.0270	−0.0150	0.0175	1.2250	0.0868
2	0.6000	0.0100	−0.0200	0.0150	1.3000	0.1284
2	0.6000	0.0100	−0.0100	0.0200	1.1500	0.1344
2	0.6000	0.0100	−0.0100	0.0200	1.3000	0.1326
2	0.6000	0.0200	−0.0200	0.0150	1.1500	0.0913
2	0.6000	0.0200	−0.0100	0.0200	1.3000	0.0911
2	0.6000	0.0200	−0.0200	0.0200	1.3000	0.0948
2	0.8000	0.0150	−0.0150	0.0175	1.2250	0.0593

Table 6 (continued)

Block	α	K_x	K_t	Δx	κ	Error L_2
2	0.8000	0.0150	–0.0150	0.0175	1.2250	0.0593

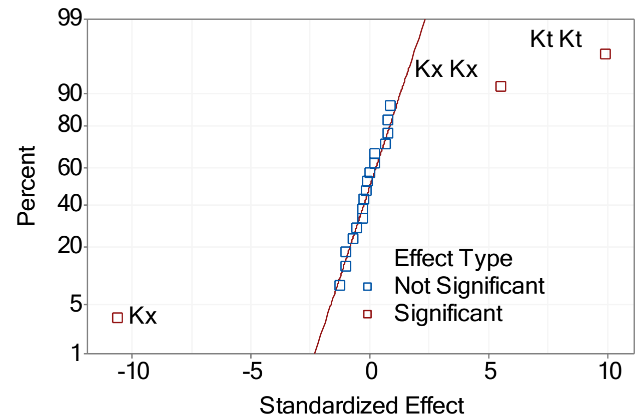

Fig. 9 Probability plot of the normalized effect of the variables

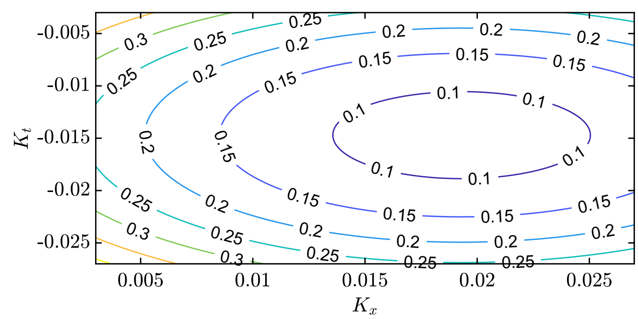

Fig. 10 Contour of simplified response surface with K_x and K_t

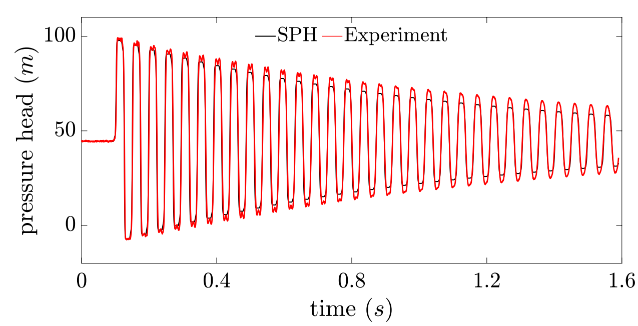

Fig. 11 Results with response surface-optimized configuration: Test 1

$$
\begin{aligned}
\langle L_2 \rangle = {} & 0.740 - 0.126\,\alpha - 33.700\,K_x + 30.600\,K_t \\
& - 7.500\,\Delta x - 0.030\,\kappa + 0.020\,\alpha^2 + \cdots \\
& \cdots + 596\,K_x^2 + 1140\,K_t^2 - 130\,\Delta x^2 - 0.01\,\kappa^2 \\
& - 2.430\,\alpha\,K_x - 3.020\,\alpha\,K_t + 7.290\,\alpha\,\Delta x - \cdots \\
& \cdots - 0.037\,\alpha\,\kappa - 40\,K_x\,K_t + 191\,K_x\,\Delta x + 6.330\,K_x\,\kappa \\
& - 89\,K_t\,\Delta x + 5.240\,K_t\,\kappa + 2.900\,\kappa\,\Delta x.
\end{aligned}
\tag{50}
$$

The values of K_x and K_t for the condition in Eq. (50) are similar to those obtained using Eq. (49), indicating the suitability of the applied statistical model. The numerical results obtained by applying the values predicted by the response surface methodology are presented in Figs. 11 and 12. The L_2 relative error obtained for Test 1 is 0.0833, and for Test 2 it is 0.0559.

Fig. 12 Results with response surface-optimized configuration: Test 2

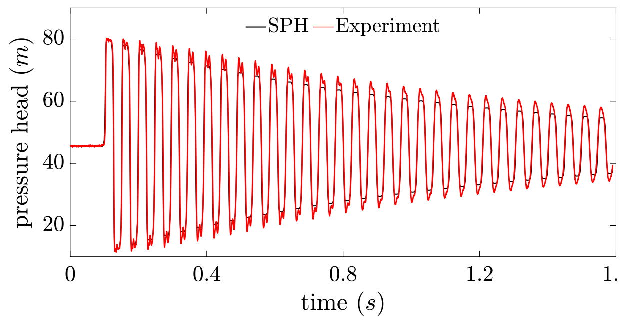

The method provides the average error value for each variable, except for the minimum value. Figures 13 and 14 show the relative mean error for each variable. K_t and K_x exhibit a global minimum due to their hyperbolic behavior. Hence, high and low values of K_t can generate a phase lag between numerical and experimental phases. Furthermore, high values of K_x dampen the numerical amplitude more intensely. Therefore, finding an optimal value to align numerical approximations with experimentation is preferred.

The number of particles in the domain is linked to the initial distance between the particles. Reducing Δx increases particle count, enhancing information resolution and accuracy. Furthermore, Δx is tied to the CFL number, ensuring numerical stability. However, domain support imbalance may cause errors. Figures 13 and 14 show the contribution of K_x and K_t to error growth. In both extreme cases, $\Delta x = 0.0116$ m and $\Delta x = 0.0225$ m, K_x and K_t were close to optimal, significantly reducing error. The κ value was 1.225 at both extremes, ensuring each boundary particle had four neighbors, forming a balanced set.

The variables α and κ behave similarly to Δx, indicating the importance of K_x and K_t in determining model accuracy. One can use the response surface to study their effect on error by fixing K_x and K_t values at the optimal point. Figure 15 shows that increasing α reduces error by intensifying the damping of spurious numerical oscillations. Reducing Δx yields more accurate results, following a slight hyperbolic trend. Finally, increasing the smoothing length control coefficient raises relative error L_2 due to an imbalance near the boundaries of compact support.

7 Conclusion

This study presents a SPH method coupled with unsteady friction models for hydraulic transient analysis. The research validated the method through experiments and numerical tests. The Corrected SPH (CSPH) technique solved domain support boundary imbalances, while the unsteady friction model by Ramos et al. (2004) showed the best results, with L_2 norm errors between 0.120 and 0.180, compared to errors in the range of (0.470, 0.540) for other models.

The parameter study revealed specific relationships between variables and model accuracy. The method showed better results with values close to unity for the artificial viscosity coefficient α within the range [0.1, 0.8]. Decreasing the initial spatial step Δx increased particle count, improving resolution and accuracy. The smoothing length, defined as $h = \kappa\,\Delta x$, showed an observed trend of increased error when increasing h values. The increment was not sufficient for the range of κ values [1.05, 1.4] to ensure an even number of particles near the pipe's edges.

Fig. 13 Average relative error L_2 of variables α and Δx

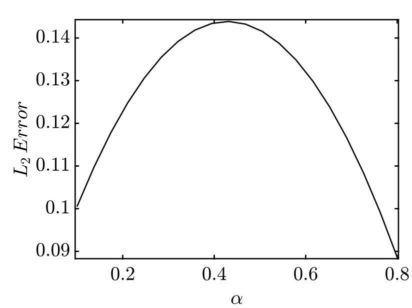

(a) Average relative L_2 error of α

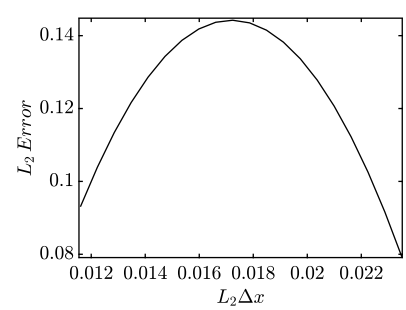

(b) Average relative L_2 error of Δx

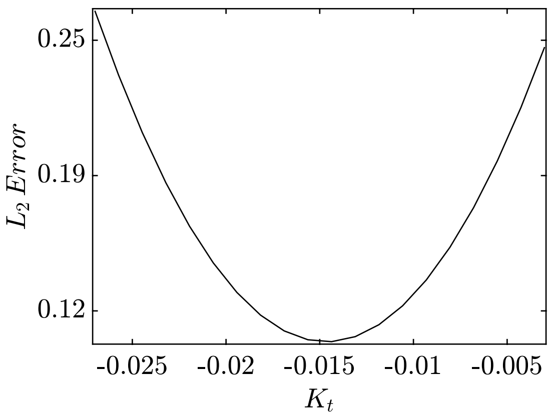

(a) Average relative L_2 error of K_t

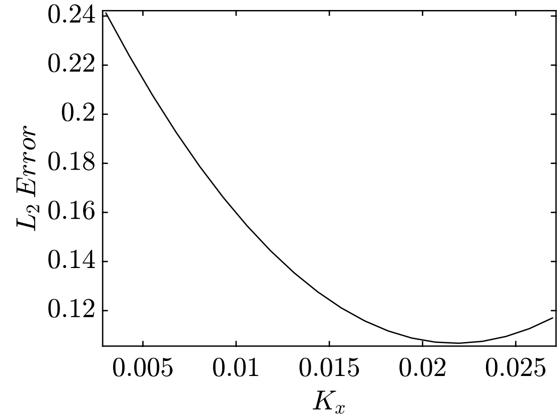

(b) Average L_2 error of K_x

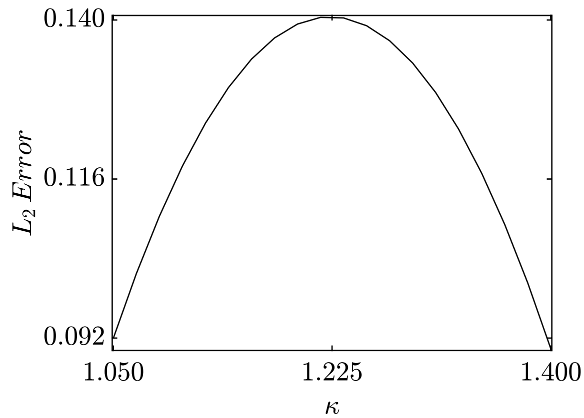

(c) Average relative L_2 error of κ

Fig. 14 Average relative error L_2 of variables K_x, K_t, and κ. the response surface method

The variables with the most influence on SPH response quality were K_x and K_t. These coefficients showed a parabolic relationship with errors, allowing the identification of global minimum values. With $\alpha = 0.8$, $K_x = 0.01997$, $K_t = -0.0149$, $\Delta x = 0.0116$, and $\kappa = 1.4$, the error prediction reached 0.0528 with 95% confidence in the range of $(-0.0422, 0.1499)$. This parabolic behavior is consistent with the physical nature of these coefficients, as their increase or decrease affects damping intensity and wave celerity.

The method has some limitations. It shows phase differences between numerical and experimental waves over long periods, particularly in regions far from the reservoir. The current version simplifies fluid–structure interaction and uses a one-dimensional approach for three-dimensional flow. The vortex sheets that form near the wall and spread radially toward the tube's center during flow inversion require three-dimensional modeling for accurate representation.

Future work should focus on coupling a viscoelastic constitutive model with the SPH method and the unsteady frictional model. This development aims to increase numerical accuracy through fluid–structure interaction without requiring full 3D unsteady flow simulation. The optimization of parameters like K_x and K_t for different flow conditions also deserves further investigation.

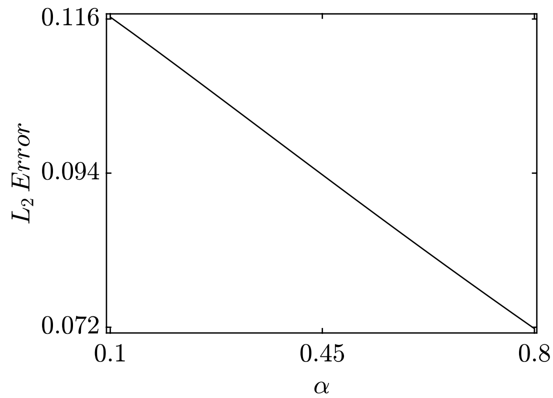

(a) Average relative L_2 error of α

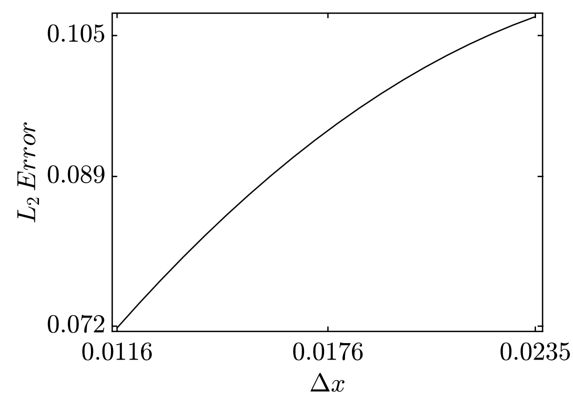

(b) Average L_2 error of Δx

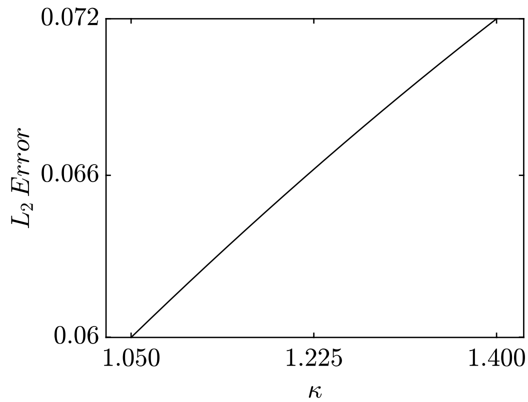

(c) Average relative L_2 error of κ

Fig. 15 Average relative error L_2 setting $K_x = 0.01997$ and $K_t = -0.0149$

This work demonstrates that combining SPH with unsteady friction models provides a practical approach for hydraulic transient analysis, particularly when proper attention is given to parameter selection and optimization.

Acknowledgements The first author is grateful to the Postgraduate Program in Mechanical Engineering (PPGMEC) at the Federal University of Goiás (UFG) for the opportunity to study and for all the support. The authors also express their gratitude to Eletrobras and the Research and Technological Development (R&D) Program for the Electric Power Sector, regulated by the National Electric Power Agency (ANEEL), for their financial support and for providing the infrastructure that made this research possible.

Author contributions A. J. V. P. S. Pamplona was responsible for drafting the manuscript and optimizing the existing codebase by reimplementing it in a more efficient programming language. He also undertook the acquisition, analysis, and interpretation of the dataset. J. F. Júnior initially developed the original version of the code. J. R. G. Vasco and A. A. Nascimento contributed by reviewing the manuscript and providing critical guidance on key intellectual aspects.

Funding The research received support through an academic scholarship, benefiting both Andreia and Joel, as well as providing essential laboratory equipment.

Data availability Access to the data and internal resources is available upon request. Interested parties can reach the primary author directly via email at almeriopamplona@gmail.com or by navigating to the repository at https://github.com/almeriopamplona..

Code availability Access to the data and internal resources is available upon request. Interested parties can reach the primary author directly via email at almeriopamplona@gmail.com or by navigating to the repository at https://github.com/almeriopamplona..

Materials availability Not applicable.

Declarations

Ethics approval and consent to participate This article does not contain any studies with human participants or animals performed by any of the authors.

Consent for publication Informed consent was obtained from all individual participants included in the study.

Competing interests The authors declare no competing interests.

References

1. Menabrea LF. Note sur les effects de choc de l'eau dans les conduites. Comptes Rendus de l'Acad des Sci. 1858;47(1):221–4.
2. Michaud J. Coups de bélier dans les conduites. Étude des moyens employés pour en atteneur les effects. Bull De La Société Vaudoise des Ingénieurs et Des Architectes. 1878;4(3):56–64.
3. Song W, Yan H, Li F, Tao T, Duan H, Xin K, Li S. Development of smoothed particle hydrodynamics based water hammer model for water distribution systems. Eng Appl Comput Fluid Mech. 2023;17(1):2171139. https://doi.org/10.1080/19942060.2023.2171139.
4. Frizell JP. Pressure resulting from changes of velocity of water in pipes. Trans Am Soc Civ Eng. 1898;39(1):1–18.
5. Joukowski NE. Memoirs of the imperial academy society of St. Petersburg. Proc Am Water Works Assoc. 1898;24(1):341–424.
6. Allievi L. Teoria generale del moto perturbato dell'acqua nei tubi in pressione. 1st ed. Rome: Assoziazione Elettrotecnica Italiana; 1903.
7. Allievi L. Allgemeine Theorie über fiber die veränderliche veranderliche Bewegung des Wassers in Leitungen. 1st ed. Berlin: Springer-Verlag; 1909.
8. Streeter VL, Wylie EB. Hydraulic transients. 1st ed. New York: McGraw-Hill; 1967.
9. Chaudhry MH. Applied hydraulic transients. 1st ed. New York: Van Nostrand Reinhold; 1987.
10. Ghidaoui MS, Zhao M, McInnis DA, Axworthy DH. A review of water hammer theory and practice. Appl Mech Rev Trans ASME. 2005;58:49–76. https://doi.org/10.1115/1.1828050.
11. Gray CAM. The analysis of the dissipation of energy in water hammer. Proc Am Soc Civ Eng. 1953;79:1176.
12. Lister M. The numerical solutions of hyperbolic partial differential equations by the method of characteristics. In: Ralston A, Wild HS, editors. Mathematical methods for digital computers. New York: John Wiley; 1960. p. 165–79.
13. Lai CA. Study of water hammer including effect of hydraulic losses, Ph.D. thesis, The University of Michigan 1961.
14. Streeter VL. Valve stroking to control water hammer. J Hydraul Div. 1963;89(2):39–66. https://doi.org/10.1061/JYCEAJ.0000862.
15. Karney BW, Ghidaoui MS. Flexible discretization algorithm for fixed-grid moc in pipelines. J Hydraul Eng. 1997;123(11):1004–11. https://doi.org/10.1061/(ASCE)0733-9429(1997)123:11(1004).
16. Bergant A, Tijsseling AS, Vítkovský JP, Covas DI, Simpson AR, Lambert MF. Parameters affecting water-hammer wave attenuation, shape and timing - part 1. J Hydraul Res. 2008;46(3):373–81. https://doi.org/10.3826/jhr.2008.2848.
17. Bergant A, Tijsseling AS, Vítkovský JP, Covas DI, Simpson AR, Lambert MF. Parameters affecting water-hammer wave attenuation, shape and timing - part 2. J Hydraul Res. 2008;46(3):382–91. https://doi.org/10.3826/jhr.2008.2847.
18. Afshar MH, Rohani M. Water hammer simulation by implicit method of characteristic. Int J Press Vessels Pip. 2008;85(12):851–9. https://doi.org/10.1016/j.ijpvp.2008.08.006.
19. Jang TU, Wu Y, Xu Y, Newman J, Sun Q. Efficient quasi-two-dimensional water hammer model on a characteristic grid. J Hydraul Eng. 2016;142(2):06016019. https://doi.org/10.1061/(ASCE)HY.1943-7900.0001219.
20. Pal S, Hanmaiahgari PR, Karney BW. An overview of the numerical approaches to water hammer modelling: the ongoing quest for practical and accurate numerical approaches. Water. 2021;13(1):1597. https://doi.org/10.3390/w13111597.
21. Song W, Yan H, Tao T, Guan M, Li F, Xin K. Modeling transient mixed flows in drainage networks with smoothed particle hydrodynamics. Water Resour Manag. 2023;38(1):861–79. https://doi.org/10.1007/s11269-023-03689-5.
22. Schönfeld JC. Resistance and inertia of the flow of liquids in a tube or open canal. Appl Sci Res. 1949. https://doi.org/10.1007/BF02120326.
23. Daily JW, Hankey WL, Olive RW, Jordaan JM. Resistance coefficients for accelerated and decelerated flows through smooth tubes and orifices. Trans ASME. 1956;78(1):1071–7. https://doi.org/10.1115/1.4013923.
24. Zielke W. Frequency-dependent friction in transient pipe flow. J Basic Eng Trans ASME. 1968;90:109–15. https://doi.org/10.1115/1.3605049.
25. Brunone B, Golia UM, Greco M. Modeling of fast transients by numerical methods, in: Proceedings of International Conference on Hydraulic Transients with Water Column Separation, 9th Round Table IAHR Group, Valencia, Madrid, 1991; pp. 273–80. https://research.unipg.it/handle/11391/137642?mode=full.
26. Vardy AE, Brown JMB. Transient, turbulent, smooth pipe friction. J Hydraul Res. 1995;33(4):435–56. https://doi.org/10.1080/00221689509498654.

27. Ramos H, Covas D, Borga A, Loureiro D. Surge damping analysis in pipe systems: modelling and experiments. J Hydraul Res. 2004;42:413–25. https://doi.org/10.1080/00221686.2004.9728407.
28. Yan H, Li S, Tian W, Wang J, Li F, Duan H, Tao T, Xin K. A hybrid model coupling data and hydraulic transient laws for water distribution systems. Water Resour Res. 2025;61(2):1–23. https://doi.org/10.1029/2023WR036641.
29. Ahmad Z, Nguyen T-K, Kim J-M. Leak detection and size identification in fluid pipelines using a novel vulnerability index and 1-d convolutional neural network. Eng Appl Comput Fluid Mech. 2023;17(1):1–17. https://doi.org/10.1080/19942060.2023.2165159.
30. Wu Y, Chi L, Zhang H. Study of resistance distribution and numerical modeling of water hammer in a long-distance water supply pipeline. In: Van Zyl JE, Hemobade AA, Jacobs HE, editors. Water distribution systems analysis 2008. Kruger National Park, Skukuza: ASCE; 2008. p. 1–10.
31. Budinski L. Application of the lbm with adaptive grid on water hammer simulation. J Hydroinform. 2016;18(4):687–701. https://doi.org/10.2166/hydro.2016.164.
32. Louati M, Mahdi Tekitek M, Salah Ghidaoui M. On the dissipation mechanism of lattice boltzmann method when modeling 1-d and 2-d water hammer flows. Comput Fluids. 2019;193(1):103996. https://doi.org/10.1016/j.compfluid.2018.09.001.
33. Lucy LB. A numerical approach to the testing of the fission hypothesis. Astron J. 1977;82:1013–24. https://doi.org/10.1086/112164.
34. Gingold RA, Monaghan JJ. Smoothed particle hydrodynamics: theory and application to non-spherical stars. Mon Not R Astron Soc. 1977;181(3):375–89. https://doi.org/10.1093/mnras/181.3.375.
35. Liu G, Liu M. Smoothed particle hydrodynamics: a meshfree particle method, 1st edn. Singapore: World Scientific Publishing Company; 2003. https://doi.org/10.1142/5340.
36. Monaghan JJ, Kos A. Solitary waves on a cretan beach. J Waterw Port Coast Ocean Eng. 1999;125(3):145–55. https://doi.org/10.1061/(ASCE)0733-950X(1999)125:3(145).
37. Colagrossi A, Colicchio G, Lugni C, Brocchini M. A study of violent sloshing wave impacts using an improved sph method. J Hydraul Res. 2010;48(sup1):94–104. https://doi.org/10.1080/00221686.2010.9641250.
38. Federico I, Marrone S, Colagrossi A, Aristodemo F, Antuono M. Simulating 2d open-channel flows through an sph model. Eur J Mech B/Fluids. 2012;34:35–46. https://doi.org/10.1016/j.euromechflu.2012.02.002.
39. Monaghan J. Simulating free surface flows with sph. J Comput Phys. 1994;110(2):399–406. https://doi.org/10.1006/jcph.1994.1034.
40. Hou Q, Kruisbrink A, Tijsseling AS, Keramat A. Simulation water hammer with corrective smoothed particle method. In: Anderson S, editor. Proceedings of 11th International Conference on Pressure Surges. Lisbon, Portugal: BHR Group; 2012. pp. 160–70. https://www.researchgate.net/publication/280623868_Simulating_water_hammer_with_corrective_smoothed_particle_method.
41. Júnior JF, Vasco JRG, Soares AK. Classical transient pipe flow analysis with sph method, in: XLI Ibero-Latin American Congress on Computational Methods in Engineering: XLI CILAMCE, Foz do Iguaçu, Parana, Brazil, 2020; 1–7. https://doi.org/https://publicacoes.softaliza.com.br/cilamce2020/article/view/6417.
42. Pan T, Zhou L, Ou C, Wang P, Liu D. Smoothed particle hydrodynamics with unsteady friction model for water hammer pipe flow. J Hydraul Eng. 2022;148(2):04021057. https://doi.org/10.1061/(ASCE)HY.1943-7900.0001966.
43. Chen JK, Beraun JE, Carney TC. A corrective smoothed particle method for boundary value problems in heat conduction. Int J Numer Methods Eng. 1999;46(2):231–52. https://doi.org/10.1002/(SICI)1097-0207(19990920)46:23.0.CO;2-K.
44. Vardy AE, Hwang K-L. A weighting function model of transient turbulent pipe friction. J Hydraul Res. 1993;31(4):533–48. https://doi.org/10.1080/00221689309498876.
45. Vítkovský JP, Lambert MF, Simpson AR, Bergnant A. Advances in unsteady friction modeling in transient pipe flow. In: Anderson A, editor. Proceedings of 8th International Conference on Pressure Surges - Safe Design and Operation of Industrial Pipe System. Hague, Netherlands: Professional Engineering Publishing Limited; 2000. pp. 471–82. http://surl.li/khzee.
46. Montgomery DC. Design and analysis of experiments. New York, USA: John Wiley & Sons Inc; 2013.
47. Soares AK, Martins NMC, Covas DIC. Transient vaporous cavitation in a horizontal copper pipe. J Hydraul Res. 2017. https://doi.org/10.1080/00221686.2017.1286394.
48. Covas DIC. Inverse transient analysis for leak detection and calibration of water pipe systems modelling special dynamic effects. Phd thesis, Imperial College London; 2003.
49. Swamee PK. Design of a submarine oil pipeline. J Transp Eng. 1993;119(1):159–70. https://doi.org/10.1061/(ASCE)0733-947X(1993)119:1(159).
50. Carstens MR, Roller JE. Boundary-shear stress in unsteady turbulent pipe flow. J Hydraul Div. 1959;85(2):67–81. https://doi.org/10.1061/JYCEAJ.0000276.
51. Monaghan JJ, Lattanzio JC. A refined particle method for astrophysical problems. Astron Astrophys. 1985;149:135–43. https://ui.adsabs.harvard.edu/abs/1985A%26A...149..135M.
52. Fulk DA, Quinn DW. An analysis of 1-d smoothed particle hydrodynamics kernels. J Comput Phys. 1996;126(1):165–80. https://doi.org/10.1006/jcph.1996.0128.
53. Monaghan JJ, Gingold RA. Shock simulation by the particle method sph. J Comput Phys. 1983;2(52):374–89. https://doi.org/10.1016/0021-9991(83)90036-0
54. Monaghan JJ. On the problem of penetration in particle methods. J Comput Phys. 1989;82(1):1–15. https://doi.org/10.1016/0021-9991(89)90032-6.
55. Martins NMC, Soares AK, Ramos HM, Covas DIC. Cfd modeling of transient flow in pressurized pipes. Comput Fluids. 2016;126:129–40. https://doi.org/10.1016/j.compfluid.2015.12.002.
56. Soares AK. Calibração e detecção de vazamentos em modelos de sistemas hidráulicos no escoamento transitório, Phd thesis, Universidade de São Paulo 2017. http://repositorio.eesc.usp.br/handle/RIEESC/1392.